

Stress-Induced Dual-Carbon Coating of $\text{Na}_3\text{V}_2(\text{PO}_4)_2\text{F}_3$ Cathode for Sodium-Ion Batteries

Yuqiang Pi, Jiajing Xiao, Lingzhi Cheng, Haoran Cheng, Xuecheng Deng, Yuxuan Ke, Xiong Yang,* and Qinyou An*

$\text{Na}_3\text{V}_2(\text{PO}_4)_2\text{F}_3$ (NVPF) has emerged as a promising candidate for SIBs cathode, but faces severe challenges, primarily due to fluorine loss and phase instability. These issues result in the formation of undesirable phases, such as $\text{Na}_3\text{V}_2(\text{PO}_4)_3$ and VF_3 , which significantly alter the electrochemical behavior of NVPF by the presence of low-voltage plateaus (≈ 3.4 V). Herein, a polytetrafluoroethylene (PTFE)-assisted sintering method that mitigates these issues is demonstrated, enabling the synthesis of phase-pure NVPF. PTFE plays a key role in this process: its viscoelastic properties induce internal stress to suppress fluorine volatilization, while its decomposition compensates fluorine loss and facilitates the formation of

another carbon layer. The optimized NVPF-4%P cathode delivers impressive capacities of 119 and 101.7 mAh g^{-1} at 0.5 and 50 C, respectively, and exhibits a long lifespan of 500 cycles with 82.1% capacity retention at 10 C. Additionally, in a full-cell configuration paired with a $\text{NaTi}_2(\text{PO}_4)_3$ anode, the system still presents excellent electrochemical performance and its potential for high-power applications. These results demonstrate that the PTFE-assisted dual-carbon coating not only mitigates fluorine loss but also ensures excellent electrochemical performance, providing a promising route for the development of high-performance SIBs cathode materials.

1. Introduction

The increasing demand for large-scale, sustainable energy storage systems has driven research into alternatives to lithium-ion batteries (LIBs), due to their high energy density, long cycle life, and relatively mature manufacturing processes. However, the widespread adoption of LIBs face severe challenges such as limited lithium resources, high production costs, and potential long-term safety risks, particularly in grid-scale applications where cost-effectiveness and resource availability are crucial.^[1–6] These limitations strongly push sodium-ion batteries (SIBs) as a promising alternative, originated from the abundance of sodium, its low production costs, and its analogous working mechanisms of LIBs.^[7–15] However, the development of high-performance SIBs is still hindered by the lack of appropriate cathode materials that simultaneously exhibit high capacity, long-term cyclability, and structural stability. Among the various candidates, polyanionic compounds such as $\text{Na}_3\text{V}_2(\text{PO}_4)_2\text{F}_3$ (NVPF) have gained considerable attention for their prominent advantages, including a robust 3D framework, high operating voltage (≈ 3.8 V versus Na^+/Na), and fast sodium-ion

diffusion kinetics.^[16–21] Despite these advantages, the practical application of NVPF is hampered by challenges in synthesizing phase-pure materials and mitigating intrinsic electronic conductivity limitations.^[12–25]

Main synthesis methods for NVPF primarily rely on high-temperature reactions to reduce V^{5+} to V^{3+} (typically above 550 °C). However, a key issue associated with this approach is the volatility of fluorine during synthesis, which inevitably results in fluorine loss and the formation of impurity phases, such as $\text{Na}_3\text{V}_2(\text{PO}_4)_3$ (NVP), Na_3VF_3 , and V_2O_3 .^[26,27] Fluorine loss directly alters the electrochemical behavior of NVPF, leading to the appearance of a low-voltage plateau at 3.4 V platform, an indication of the NVP impurity phase.^[28–31] This impurity phase not only accelerates capacity fade during long-term cycling, but also significantly limits the energy density due to the reduction in working potential.^[32–34] These issues underscore the critical role of fluorine in the electrochemical performance of NVPF, highlighting the necessity of maintaining the ideal stoichiometric ratio during its synthesis. To address these challenges, various strategies have been proposed, including carbon coating and structural optimization.^[35–38] However, fluorine loss remains a persistent problem in the synthesis of NVPF. This can be primarily attributed to the volatilization of fluorine ions at elevated temperatures, which is exacerbated by the mismatch in thermal expansion coefficients between NVPF and carbon precursors during high-temperature treatment. This mismatch induces internal stress, microcracks, and delamination, which compromise the structural integrity of the material. Interestingly, the concept of internal stress engineering, commonly applied in the synthesis of ceramic materials and ceramic-based solid-state electrolytes, presents a promising solution.^[39–43] In ceramics, controlled internal stress is employed to enhance densification, prevent grain boundary cracking, and tailor mechanical properties.^[44] Notably, this approach is rarely explored in SIBs

Y. Pi, J. Xiao, L. Cheng, H. Cheng, X. Deng, Y. Ke, X. Yang

School of Chemistry and Materials Science
Hubei Engineering University
Hubei, Xiaogan 432000, China
E-mail: yangx@hbeu.edu.cn

Q. An
State Key Laboratory of Advanced Technology for Materials Synthesis and Processing
Wuhan University of Technology
Hubei, Wuhan 430070, China
E-mail: anqinyou86@whut.edu.cn

 Supporting information for this article is available on the WWW under <https://doi.org/10.1002/batt.202500325>

cathode synthesis, particularly for fluorine-containing polyanionic materials.

In this work, we propose a novel internal stress-assisted sintering strategy to fabricate pure-phase NVPF cathodes with a dual-layer carbon encapsulation. By designing a carbon-thermal reduction process under precisely controlled stress conditions, it is demonstrated that the inherent stress generated during crystallization can be harnessed to drive the spontaneous formation of a dual-carbon architecture. This unique strategy not only suppresses fluorine loss and impurity phase formation but also establishes a resilient conductive network that accommodates volume changes during cycling. The resulting material achieves the remarkable capacities of 119 and 101.7 mAh g⁻¹ at 0.5 and 50 C, respectively, and exhibits a long lifespan of 500 cycles with 82.1 % capacity retention at 10 C. Furthermore, when paired with a NaTi₂(PO₄)₃ (NTP) anode in a full-cell configuration, the dual-carbon coated NVPF still exhibit excellent performance, highlighting its practical viability. By bridging the gap between innovations in materials synthesis and electrochemical performance, this work establishes a universal framework for designing stress-optimized electrode materials, thereby paving the way for high-energy, durable SIBs.

2. Experimental Section

2.1. Synthesis of Pure-Phase NVPF with a Dual-Carbon Layer

The pure-phase NVPF with a dual-carbon layer cathode material was synthesized via a two-step sintering process combined with a

stress-induced strategy (Figure 1). The detailed procedure is as follows.

654 g of V₂O₅, 454 g of NaF, 828 g of NH₄H₂PO₄, and 400 g of glucose (C₆H₁₂O₆, carbon source) were mixed in a methanol solvent. The mixture was subjected to ball-milling for 3 h to ensure homogeneous dispersion. The slurry obtained after ball milling was spray-dried at 200 °C to obtain a precursor powder, which was then calcined under a nitrogen (N₂) atmosphere at 350 °C for 5 h. To induce internal stress and enhance particle-to-particle adhesion, 4 wt% polytetrafluoroethylene (PTFE) was uniformly blended with the pre-sintered precursor powder. The resulting mixture was pressed into cylindrical pellets under 20 MPa pressure for 30 s to introduce mechanical stress on the particle interfaces, promoting densification and alignment of the carbon precursor during the subsequent sintering process. The pellets were sintered at 600 °C for 8 h under N₂, then crushed and sieved (200 mesh) to obtain the final samples, labeled as NVPF-4%P. For comparative analysis, 0%, 1%, and 2% PTFE were used, with the corresponding samples labeled as NVPF, NVPF-1%P, and NVPF-2%P, respectively.

This method integrated ceramic stress-engineering strategies with battery material design, providing a universal pathway for the development of pure-phase, high-stability F-based polyanionic cathode. The incorporation of PTFE during the pellet pressing and sintering processes served several key functions: 1) The unique viscoelastic properties of PTFE allowed it to act as a stress-inducing binder during pellet pressing. Under mechanical compression, PTFE formed an adhesive network between precursor particles, creating localized internal stresses at particle interfaces. These stresses persisted throughout the sintering process, playing a

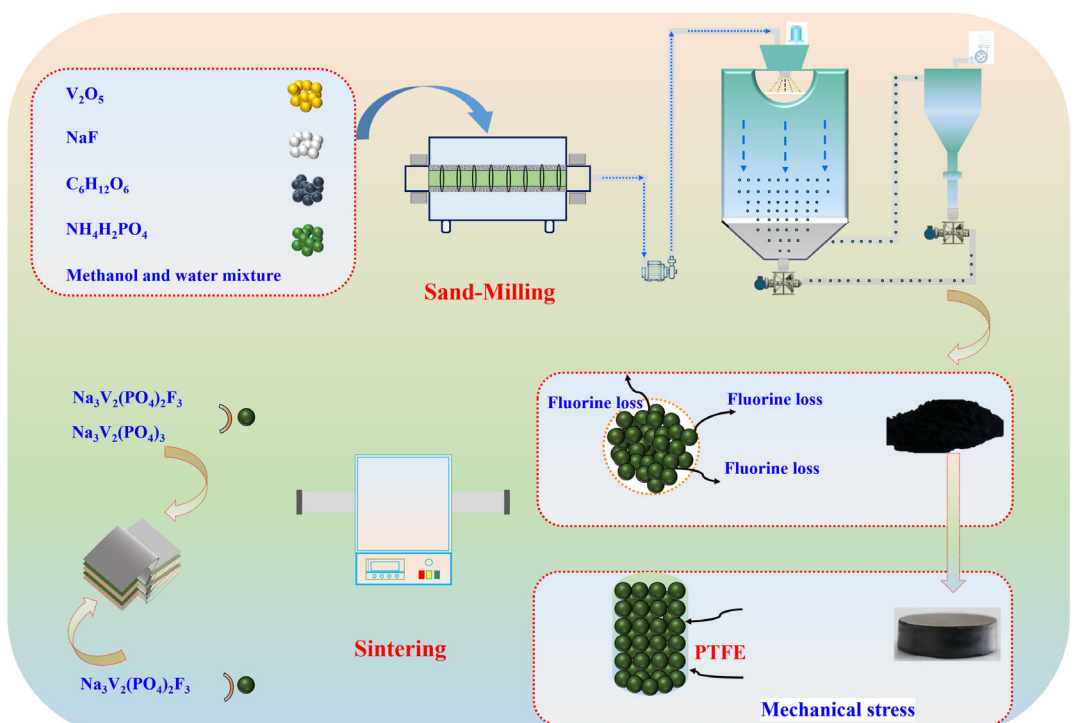


Figure 1. Schematic illustration of the synthesis process of pure-phase NVPF.

crucial role in suppressing fluoride volatilization by densifying the pellet structure. PTFE reduced pore connectivity, thereby physically obstructing pathways for fluorine loss. 2) Due to its high fluorine content, PTFE compensated for the fluoride ion loss induced by elevated temperatures, thereby maintaining the chemical stability of the material. 3) Under high-temperature conditions, PTFE decomposed into amorphous carbon, which contributed to the formation of a dual-carbon layer. This dual-layer structure not only further mitigated fluoride ion volatilization but also significantly enhanced the electronic conductivity of the electrode material.

2.2. Material Characterization

X-ray diffraction (XRD) analysis was conducted using a Bruker D8 advanced powder X-ray diffractometer with a Cu K α X-ray source to obtain crystal structure information. Raman spectra were acquired using a Renishaw IN VIA micro-spectroscopy system. A Vario EL cube CHNSO elemental analyzer was used to determine the carbon contents. The Brunauer–Emmett–Teller (BET) surface area was characterized with a Tristar II 3020 instrument by nitrogen adsorption at 77 K. Elemental valence states were determined using an Ultra DLD with a monochromatic Al X-ray source. Sample morphology was observed with a JEOL-7100F scanning electron microscope (SEM) equipped with energy-dispersive X-ray spectroscopy (EDS) analysis, while detailed structural information was obtained using a JEM-2100F transmission electron microscope (TEM).

2.3. Electrochemical Testing

The sequential processing steps for the NVPF cathode and NTP (Hubei Energy Co., Ltd.) anode included mixing, coating, drying,

and cutting. First, a mass ratio of 8:1:1 was used for the active material, conductive carbon nanotubes slurry, and polyvinylidene fluoride (PVDF, binder), respectively. After adding an appropriate amount of N-methyl-2-pyrrolidone (NMP) solvent, a uniform slurry with suitable viscosity was obtained by mixing for 1 h. This slurry was then coated onto Al foils with a carbon layer. The coated electrodes were dried at 105 °C for 12 h. Subsequently, the NVPF and NTP electrodes were cut into discs with diameters of 10 mm and 12 mm, respectively. The areal density of the NVPF cathode was adjusted to $\approx 3 \text{ mg cm}^{-2}$, and the N/P ratio between the NVPF cathode and NTP anode was controlled at 1:1.1–1.2 to optimize the electrochemical performance of the NVPF//NTP Na-ion full battery. To demonstrate the electrochemical performance of the NVPF cathode, Na metal was used as the anode and counter electrode. The electrolyte consisted of 1 M NaClO₄ in a solution of ethylene carbonate (EC) and dimethyl carbonate (DMC) (1:1 by volume) with an additional 5 vol% fluoroethylene carbonate (FEC). A Whatman glass microfiber filter (Grade GF/A) was employed between the cathode and anode to prevent direct contact. The 2025-coin cells were assembled in a glove box filled with ultra-pure Ar gas. The electrochemical performance was characterized using the LAND CT2001A battery test system and the CHI 760e electrochemical workstation for cyclic voltammetry (CV) measurements

3. Result and Discussion

To investigate the effect of PTFE content on the crystal structure, comparative XRD patterns are shown in Figure 2a, where NVPF-4%P sample shows well-defined diffraction peaks corresponding to the single orthorhombic Na₃V₂(PO₄)₂F₃ phase. Notably, the broader

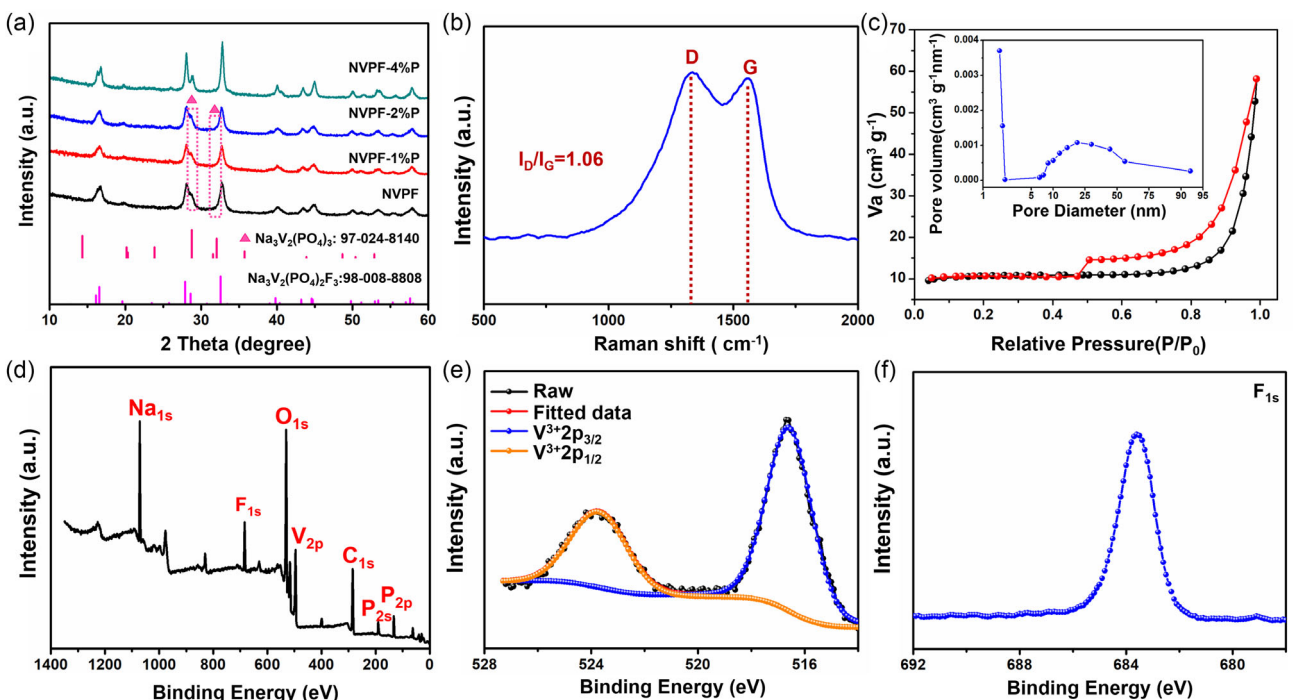


Figure 2. The structural information of NVPF-4%P. a) The contrastive XRD patterns, b) Raman spectra, c) nitrogen adsorption-desorption isotherm and corresponding pore size distribution (inset) (c), d) full XPS spectrum, e) V 2p fine spectrum, and f) F 1s fine spectrum.

peaks can be observed in the other samples, ascribed to the superposition from (024) plane of $\text{Na}_3\text{V}_2(\text{PO}_4)_3$ impurity and (113) plane of NVPF. The disappearance of impurity peaks in the NVPF-4%P sample emphasizes the effectiveness of the PTFE-induced fluorine retention. Raman spectra (Figure 2b) confirm the existence of carbon layer coating on the NVPF-4%P sample. The peaks at around 1333.9 cm^{-1} and 1556.5 cm^{-1} correspond to the D and G bands of carbon, and the value of I_D/I_G is calculated to be about 1.06, implying a well-balanced carbon structure of NVPF-4%P sample with the improved electron conductivity. The carbon content analysis shows that 5.25% of carbon is coated on the NVPF-4%P sample, while the NVPF sample without PTFE contains $\approx 4.9\%$ carbon. This indicates that the addition of PTFE distinctly contributes to the overall carbon content of the material. Figure 2c shows the BET surface area analysis of the NVPF-4%P sample, revealing a specific surface area of $32.1 \text{ m}^2 \text{ g}^{-1}$ with the dominating 25 nm pore size. A higher surface area typically facilitates better electrolyte penetration and ion transport, which is crucial for improving the rate capability of the material. Figure 2d presents the XPS spectrum of NVPF-4%P, revealing the corresponding valence state of P 2p, P 2s, C 1s, V 2p, O 1s, F 1s, and Na 1s. The fine vanadium spectrum (Figure 2e) shows the characteristic peaks associated with the V^{3+} oxidation states in NVPF,

confirming the correct valence state of vanadium in the material. This analysis demonstrates that the V^{5+} from the raw V_2O_5 material has been fully reduced, supporting the high-phase purity of the synthesized material. Finally, the fluorine spectrum (Figure 2f) confirms the presence of fluorine in the sample. Collectively, the structural characterization results validate the success of the synthesis process in achieving a pure-phase, stable $\text{Na}_3\text{V}_2(\text{PO}_4)_2\text{F}_3$ phase with minimal impurity formation.

The morphological characteristics of the NVPF-4%P cathode material were systematically investigated using high-resolution scanning electron microscopy (HRSEM) and transmission electron microscopy (TEM). The NVPF-4%P sample exhibits segmental microspheres, which are formed through the spray-drying method. Mechanical stress was applied to break the microspheres into irregular particle morphology (Figure 3a). For NVPF sample, which was not subjected to mechanical pressure, a completely spherical morphology is observed in Figure S1, Supporting Information. EDS mapping (Figure 3c) confirms the homogeneous distribution of Na, V, P, F, and C elements across the NVPF particles. TEM images (Figure 3d) provide a clearer view of the NVPF cathode's internal structure, showing that NVPF nanoparticles are interconnected by amorphous carbon resulting from the pyrolysis of PTFE during the

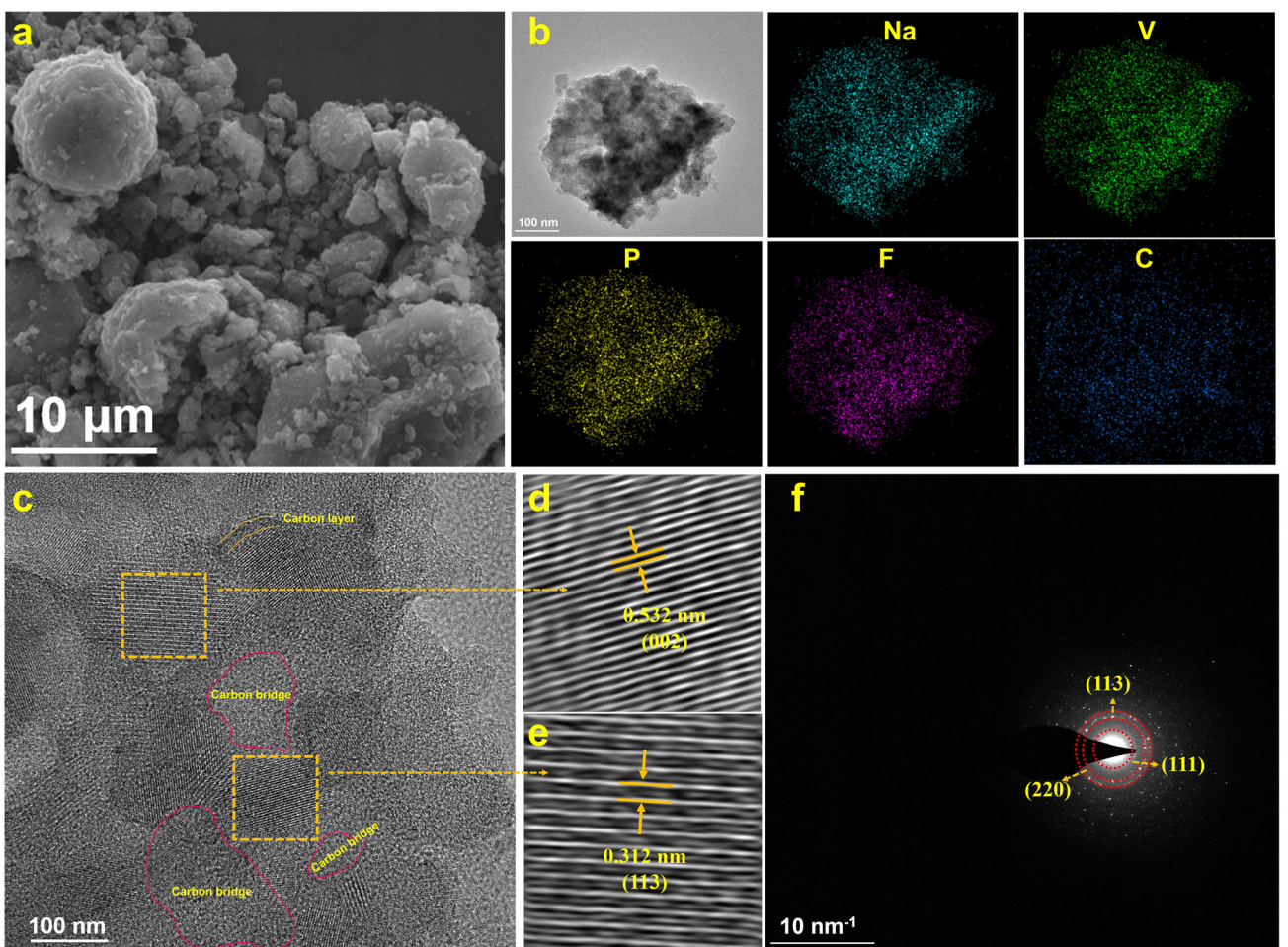


Figure 3. a,b) SEM images of NVPF-4%P sample. The EDS mappings accompanied with diagram of (b); c) HRTEM; d,e), FFT of NVPF-4%P; f) the corresponding SAED patterns of NVPF-4%P.

sintering process. Additionally, glucose undergoes in situ reduction to form a carbon layer that coats the NVPF surface, contributing to the dual-layer carbon encapsulation structure. Well-defined lattice fringes with d-spacings of 0.532 nm and 0.312 nm are observed, corresponding to the (002) and (113) planes of the NVPF phase, respectively. The selected area electron diffraction (SAED) pattern (inset of Figure 3f) clearly shows the diffraction rings indexed to the rhombohedral NVPF phase, corresponding to the (113), (220), and (111) planes.

The electrochemical behavior of the NVPF samples was systematically investigated for elucidating the effect of pure phase on electrochemical performance. The CV profiles (Figure 4a) reveal a critical difference in electrochemical behavior. Evidently, a distinct redox pair at ≈ 3.4 V could be observed, attributed to the Na^+ (de)intercalation in impurity phases NVP. Notably, the peak strength gradually decreases until the peak disappears with the increased PTFE content to 4%, which is consistent with the results of $D_{\text{Q}}/D_{\text{V}}$ in Figure S2, Supporting Information. The galvanostatic charge/discharge profiles at 0.5 C demonstrate the absence of the 3.4 V plateau for NVPF-4%P, confirming the preservation of the pure-phase phase of NVPF. Figure 4c compares the difference in rate performance, and NVPF-4%P sample shows the capacities of 120, 112.6, 108.2, 107.3, 103.1, and 101.7 mAh g^{-1} at current densities of 1, 5, 10, 20, 30, and 50 C, respectively, significantly higher than other samples. Furthermore, 92.1% of the original discharge capacity was recovered when the current density was returned to 1C, indicative of excellent reversibility. Remarkably, the capacitive effects induced by the dual-carbon coating may be a significant factor contributing to the exceptional power capability.^[45,46] Additionally, NVPF-4%P delivers 119 mAh g^{-1} at 0.5 C and 106.6 mAh g^{-1} at 10 C. After cycling for 100 and 500

cycles, the capacity retentions are 88.1% and 82.1%, respectively. These results demonstrate that the existence of low-voltage plateaus from the NVP phase slows down the kinetics properties and damages electrochemical performance of the NVPF cathodes. In other words, the strategy of stress-induced fluorine stabilization plays a crucial role in enhancing the kinetics of NVPF cathodes, while also maintaining the material's structural integrity during high-rate cycling. This is especially important for preventing delamination and cracking. Together, these improvements contribute to the superior electrochemical performance of the dual-carbon coated NVPF.

To further investigate the role of induced stress and F^- compensation in the electrochemical performance of NVPF cathodes, we conducted a series of comparative experiments. One set involved adding 6% PTFE without applying mechanical pressure (Figure S3, Supporting Information), while another set employed a 4% PEO binder (Figure S4, Supporting Information). In both cases, the resulting samples exhibited redox peaks and charge–discharge plateaus characteristic of the NVP phase, indicative of impurity-related electrochemical behavior. Specifically, the presence of these peaks suggests incomplete fluorine retention and the formation of impurity phases, both of which adversely affect electrochemical performance. These samples demonstrated significantly lower capacities and reduced cycling stability compared to the pure-phase NVPF cathodes, emphasizing the critical impact of phase purity on electrochemical behavior. These findings underscore the essential roles of both appropriate mechanical pressure and PTFE incorporation in synthesizing pure-phase NVPF cathodes. PTFE plays a pivotal role in fluorine retention during the sintering process, while the applied pressure ensures the formation of a dense and uniform microstructure. Together, these factors prevent

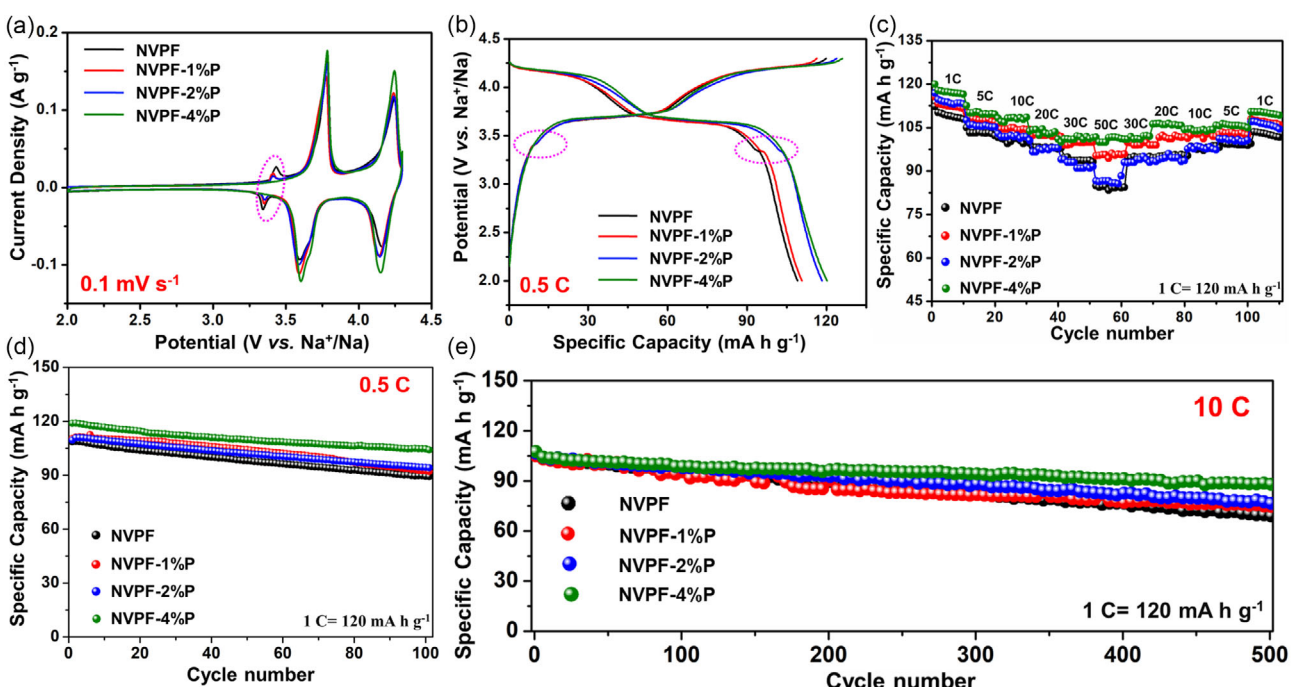


Figure 4. The corresponding electrochemical performance of NVPF samples pressed with different contents of PTFE; a,b) the CV and charge-discharge curves, respectively; c) rate performance; d,e) cyclic performance at 0.5 and 10 C, respectively.

the formation of impurity phases, enhance the structural integrity of the NVPF material, and optimize its electrochemical performance. Without either of these elements, the material fails to achieve the desired purity, resulting in suboptimal electrochemical performance.

Ex situ XRD analysis was performed on the NVPF-4%P electrode to investigate the structural evolution during the first charge and discharge cycle (2–4.3 V). As shown in **Figure 5**, the diffraction peaks at 20 values of 27.5° and 28.3° correspond to the characteristic (220) and (110) planes of NVPF in the original state, respectively. Upon charging to 4.3 V, these peaks shift to higher angles, indicating a change in the crystal structure. Notably, no diffraction peaks disappear, and no new peaks

emerge. This shift is attributed to the deintercalation of two Na^+ ions from the NVPF crystal structure, resulting in a decrease in the layer spacing. During the discharge process to 2 V, corresponding to Na^+ re-intercalation, these peaks return to their original positions, confirming full lattice recovery with negligible hysteresis. This behavior demonstrates the excellent structural stability of the NVPF electrode throughout the charge/discharge cycle.

To further explore the feasibility of practical applications, a Na-ion full cell (NIFC) was designed and assembled, integrating the NVPF cathode and NTP anode. As illustrated in **Figure 6a**, during the charging process, sodium ions are deintercalated from the NVPF cathode and intercalated into the NTP anode. During

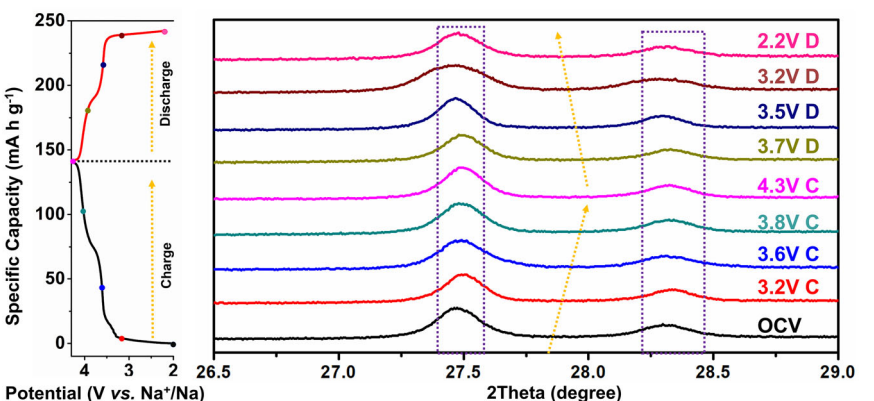


Figure 5. Ex situ XRD characterization of NVPF-4%P electrode at various states of charge and discharge in Na-ion half cells, respectively.

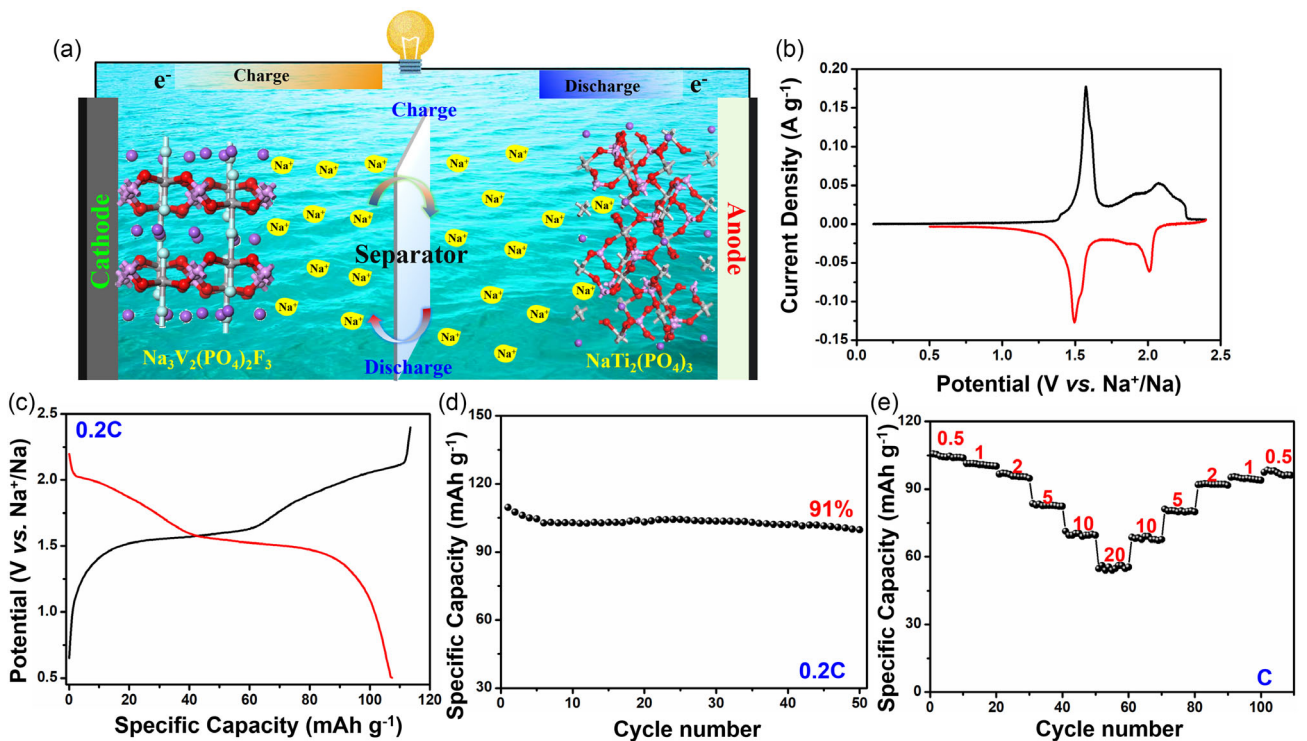


Figure 6. The relevant electrochemical performance of the NVPF//NTP full cells. a) Schematic diagram of the working mechanism of full cells; b) CV curve at 0.1 mV s^{-1} ; c,d) the charge-discharge curve and cycling performance at 0.2 C , respectively; e) rate performance.

discharge, the reverse process occurs, with sodium ions migrating back to the NVPF cathode. The working mechanism of the full cell can be explained by the following reaction equation

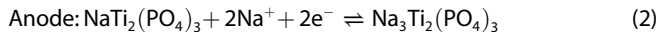
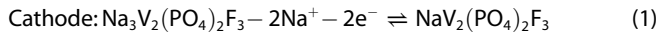


Figure 6b presents the cyclic voltammetry (CV) curves of the full-cell at a scan rate of 0.1 mV s^{-1} where two well-defined redox peaks are observed, corresponding to the Na^+ intercalation and de-intercalation processes between the NVPF cathode and the NTP anode. The charge and discharge profiles (Figure 6c) exhibit two characteristic plateaus at a current rate of 0.2 C , which are consistent with the CV results. The symmetric peaks and clear plateaus indicate good reversibility and fast kinetics for sodium-ion transfer between the electrodes. The cycling performance of the full-cell was evaluated at a rate of 0.2 C , as shown in Figure 6d. The NVPF//NTP full-cell demonstrated excellent cycling stability, retaining 91% of its initial capacity (109.6 mAh g^{-1}) after 50 cycles. The minimal capacity fade is attributed to the effective suppression of fluorine loss and the enhanced stability provided by the dual-layer carbon coating. Furthermore, Figure 6e presents the rate performance of the full cell at different C-rates, ranging from 0.5 C to 20 C . Capacities of 105.6 , 101.4 , 97 , 83.6 , 71.3 , and 54.7 mAh g^{-1} are achieved at 0.5 , 1 , 2 , 5 , 10 , and 20 C , respectively. When the current density is reduced back to 0.5 C , a capacity of 98.4 mAh g^{-1} is recovered. These results demonstrate that the NVPF//NTP Na-ion full cells exhibit excellent power capability, highlighting their potential for high-power applications such as electric vehicles and grid energy storage. The outstanding performance can be attributed to the pure-phase nature of the NVPF material and the enhanced conductivity facilitated by the dual-layer carbon coating.

4. Conclusion

This study introduces a novel internal stress-assisted sintering strategy to fabricate pure-phase $\text{Na}_3\text{V}_2(\text{PO}_4)_2\text{F}_3$ cathode with dual-layer carbon encapsulation. By leveraging the triple functionality of PTFE—as a stress generator, dynamic fluorine compensator, and carbon precursor, this approach addresses the persistent challenges of fluorine loss and phase impurities in NVPF cathode. The introduction of 4% PTFE enables the synthesis of pure-phase NVPF, which demonstrates superior electrochemical performance, including a high discharge capacity of 119 mAh g^{-1} at 0.5 C , outstanding rate capability of 101.7 mAh g^{-1} at 50 C , and excellent cycling stability with 82.1% capacity retention over 500 cycles at 10 C . When paired with the NTP anode in NIFCs, the NVPF- 4% P electrode shows remarkable electrochemical performance, highlighting its potential for high-power applications. These results demonstrate that the stress-induced strategy not only facilitates the synthesis of dual-carbon, pure-phase $\text{Na}_3\text{V}_2(\text{PO}_4)_2\text{F}_3$ cathode, but also enhances the electrochemical performance of the final samples. This scalable and cost-effective method offers a promising pathway for the development of next-generation

sodium-ion batteries, exhibiting high capacity, excellent power capability, and extended cycle life.

Acknowledgements

This work was supported by the Key Research and Development Program of Hubei (2022BAA027).

Conflict of Interest

The authors declare no conflict of interest.

Data Availability Statement

The data that support the findings of this study are available from the corresponding author upon reasonable request.

Keywords: dual-layer carbon coating • fluorine loss • high performance • $\text{Na}_3\text{V}_2(\text{PO}_4)_2\text{F}_3$ • PTFE-assisted sintering

- [1] J. B. Goodenough, K. S. Park, *J. Am. Chem. Soc.* **2013**, *135*, 1167.
- [2] B. Dunn, H. Kamath, J. M. Tarascon, *Science* **2011**, *334*, 928.
- [3] M. Armand, J. M. Tarascon, *Nature* **2008**, *451*, 652.
- [4] J. M. Tarascon, *Joule* **2020**, *4*, 1616.
- [5] W. Mrozik, M. A. Rajaeifar, O. Heidrich, P. Christensen, *Energ. Environ. Sci.* **2021**, *14*, 6099.
- [6] H. Z. Wang, L. Y. Zhao, H. Zhang, Y. S. Liu, L. Yang, F. Li, W. H. Liu, X. T. Dong, X. K. Li, Z. H. Li, X. D. Qi, L. Y. Wu, Y. F. Xu, Y. Q. Wang, K. K. Wang, H. C. Yang, Q. Li, S. S. Yan, X. G. Zhang, F. Li, H. S. Li, *Energ. Environ. Sci.* **2022**, *15*, 311.
- [7] W. Lee, J. Kim, S. Yun, W. Choi, H. Kim, W. S. Yoon, *Energ. Environ. Sci.* **2020**, *13*, 4406.
- [8] C. Sun, L. L. Zhang, X. Q. Xiong, Z. R. Deng, H. B. Sun, X. L. Yang, *ACS Sustain. Chem. Eng.* **2024**, *12*, 10892.
- [9] H. M. Yi, L. Lin, M. X. Ling, Z. Q. Lv, R. Li, Q. Fu, H. M. Zhang, Q. Zheng, X. F. Li, *ACS Energy Lett.* **2019**, *4*, 1565.
- [10] F. Duffner, N. Kronemeyer, J. Tübke, J. Leker, M. Winter, R. Schmuck, *Nat. Energy* **2021**, *6*, 123.
- [11] N. Yabuuchi, K. Kubota, M. Dahbi, S. Komaba, *Chem. Rev.* **2014**, *114*, 11636.
- [12] G. Y. Wan, W. D. Dou, H. Y. Zhu, W. Zhang, T. F. Liu, L. G. Wang, J. Lu, *Interdiscip. Mater.* **2023**, *2*, 416.
- [13] X. J. Luo, Q. X. Liu, L. Lei, W. Xia, Y. M. Yin, X. Q. Wu, C. H. Yang, R. Chi, D. S. Li, *Surf. Interfaces* **2025**, *63*, 106259.
- [14] Z. Y. Gu, X. T. Wang, Y. L. Heng, K. Y. Zhang, H. J. Liang, J. L. Yang, E. H. Ang, P. F. Wang, Y. You, F. Du, X. L. Wu, *Sci. Bull.* **2023**, *68*, 2302.
- [15] Y. M. Yin, C. Y. Pei, W. Xia, X. J. Luo, D. S. Li, *Small* **2023**, *19*, 2303666.
- [16] C. Sun, L. L. Zhang, Z. R. Deng, H. B. Sun, X. L. Yang, *ACS Appl. Mater. Inter.* **2024**, *16*, 35179.
- [17] J. Wang, Q. M. Liu, S. Y. Cao, H. J. Zhu, Y. L. Wang, *J. Colloid Interf. Sci.* **2024**, *665*, 1043.
- [18] Y. U. Park, D. H. Seo, H. S. Kwon, B. Kim, J. Kim, H. Kim, I. Kim, H. I. Yoo, K. Kang, *J. Am. Chem. Soc.* **2013**, *135*, 13870.
- [19] C. Guo, J. W. Yang, Z. Y. Cui, S. Qi, Q. Q. Peng, W. W. Sun, L. P. Lv, Y. Xu, Y. Wang, S. Q. Chen, *J. Energy Chem.* **2022**, *65*, 514.
- [20] S. L. Chou, Y. Yu, *Adv. Energy Mater.* **2017**, *7*, 1703223.
- [21] J. Miranda, P. L. Taberna, P. Simon, *ACS Nano* **2025**, *19*, 2419.
- [22] S. Q. Chen, C. Wu, L. F. Shen, C. B. Zhu, Y. Y. Huang, K. Xi, J. Maier, Y. Yu, *Adv. Mater.* **2017**, *29*, 1700431.
- [23] X. Shen, Q. Zhou, M. Han, X. G. Qi, B. Li, Q. Q. Zhang, J. M. Zhao, C. Yang, H. Z. Liu, Y. S. Hu, *Nat. Commun.* **2021**, *12*, 2848.
- [24] Z. L. Jian, Y. S. Hu, X. L. Ji, W. Chen, *Adv. Mater.* **2017**, *29*, 1601925.
- [25] M. Bianchini, F. Fauth, N. Brisset, F. Weill, E. Suard, C. Masquelier, L. Croguennec, *Chem. Mater.* **2015**, *27*, 3009.
- [26] L. Deng, F. D. Yu, Y. Xia, Y. S. Jiang, X. L. Sui, L. Zhao, X. H. Meng, L. F. Que, Z. B. Wang, *Nano Energy* **2021**, *82*, 105659.

- [27] X. H. Wu, W. J. Jiang, C. Dai, L. Z. Liu, Y. Chai, M. J. Zhao, L. B. Yang, Y. Lin, Y. Zhao, W. Huang, *Adv. Mater.* **2025**, *37*, 2414358.
- [28] Y. Q. Pi, J. J. Xiao, Y. T. Liu, K. K. Feng, L. Y. Xiong, J. Liu, F. Wang, C. X. Dong, Y. Ding, X. Xu, *J. Energy Storage* **2025**, *113*, 115593.
- [29] Q. Zheng, H. M. Yi, X. F. Li, H. M. Zhang, *J. Energy Chem.* **2018**, *27*, 1597.
- [30] R. S. Kate, H. S. Jadhav, U. P. Chothe, K. Bhattacharjee, M. V. Kulkarni, R. J. Deokate, B. B. Kale, R. S. Kalubarme, *J. Mater. Chem. A* **2024**, *12*, 7418.
- [31] J. Liu, B. Li, Q. Y. Li, W. Fu, M. Y. Wang, Z. Y. Lin, F. Z. Jiang, K. X. Zhu, L. Y. Yang, F. F. Li, P. Wang, *Chem. Eng. Sci.* **2024**, *295*, 120187.
- [32] Q. X. Hu, M. J. Sun, Y. C. Zha, G. Q. Zhao, H. L. Tang, L. Yang, M. Yang, B. H. Pang, Y. J. Sun, H. Guo, *ACS Energy Lett.* **2025**, *10*, 1840.
- [33] Y. Jiang, Y. Yang, F. X. Ling, G. X. Lu, F. Y. Huang, X. Y. Tao, S. F. Wu, X. L. Cheng, F. F. Liu, D. J. Li, H. Yang, Y. Yao, P. C. Shi, Q. W. Chen, X. H. Rui, Y. Yu, *Adv. Mater.* **2022**, *34*, 2109439.
- [34] Y. S. Cai, X. X. Cao, Z. G. Luo, G. Z. Fang, F. Liu, J. Zhou, A. Q. Pan, S. Q. Liang, *Adv. Sci.* **2018**, *5*, 1800680.
- [35] J. K. Ou, H. Wang, H. W. Zhang, S. G. Wu, W. Wang, L. Zou, F. Jin, *J. Power Sources* **2021**, *516*, 230654.
- [36] Y. Zhang, T. Wang, Y. K. Tang, Y. D. Huang, D. Z. Jia, Y. Guo, Z. Zhou, *J. Power Sources* **2021**, *516*, 230515.
- [37] Y. Y. Qin, L. Li, H. Y. Zhao, M. Y. Wang, X. Y. Li, J. Zhao, H. Wu, S. J. Ding, *Crystengcomm* **2022**, *24*, 4519.
- [38] D. Ma, L. L. Zhang, T. Li, C. Liu, G. Liang, Y. X. Zhou, X. L. Yang, *Electrochim. Acta* **2018**, *283*, 1441.
- [39] X. X. Wang, Z. H. Liu, Y. H. Tang, J. J. Chen, D. J. Wang, Z. Y. Mao, *J. Power Sources* **2021**, *481*, 228924.
- [40] Z. D. Yang, B. Tang, Z. J. Xie, Z. Zhou, *Chemelectrochem* **2021**, *8*, 1035.
- [41] J. Y. Yang, Z. H. Gao, T. Ferber, H. F. Zhang, C. Guhl, L. T. Yang, Y. Y. Li, Z. Deng, P. R. Liu, C. W. Cheng, R. C. Che, W. Jaegermann, R. Hausbrand, Y. H. Huang, *J. Mater. Chem. A* **2020**, *8*, 7828.
- [42] J. A. S. Oh, L. C. He, A. Plewa, M. Morita, Y. Zhao, T. Sakamoto, X. Song, W. Zhai, K. Y. Zeng, L. Lu, *ACS Appl. Mater. Inter.* **2019**, *11*, 40125.
- [43] J. H. Ma, X. H. Zu, X. Q. Qiu, W. L. Zhang, *Chem. Eng. J.* **2024**, *493*, 152792.
- [44] F. Q. Lu, Y. D. Lu, L. Z. Zhao, *J. Power Sources* **2025**, *645*, 237194.
- [45] Y. Lu, J. A. Alonso, Q. Yi, L. Lu, Z. L. Wang, C. W. Sun, *Adv. Energy Mater.* **2019**, *9*, 1901205.
- [46] L. X. Zhang, Y. M. Liu, Y. You, A. Vinu, L. Q. Mai, *Interdiscip. Mater.* **2023**, *2*, 91.

Manuscript received: April 29, 2025

Revised manuscript received: June 6, 2025

Version of record online: